



School of Physics and Astronomy
University of Birmingham

Supervisors: Graham Smith, Alistair Sanderson, Melissa Gillone

Abstract

[illegible]

Contents

| | |
|--|-----------|
| Contents | 3 |
| 1 Introduction | 4 |
| 1.1 Why Investigate Cosmic Re-Ionisation | 4 |
| I General Theory | 5 |
| 2 Gravitational Lensing | 5 |
| 2.1 Introduction | 5 |
| 2.2 Concept | 6 |
| II Predictions | 9 |
| 3 Predictions Group | 9 |
| 4 Assumptions Made | 9 |
| 5 Parameter Values | 10 |
| 5.1 Parameter Evolution | 11 |
| 6 Cosmological Distances | 11 |
| 7 Schechter Function | 12 |
| 7.1 Number of Galaxies | 13 |
| 7.2 Star Formation Rate | 14 |
| III Observations | 15 |
| 8 Observing Strategy Group | 15 |
| 9 Determining Redshift | 16 |
| 9.1 Filters and the Dropout Technique | 16 |
| 10 The Hubble Space Telescope | 18 |
| 10.1 Mission Launch | 18 |
| 10.2 Achievements to Date | 19 |
| 10.3 Operation | 19 |
| 10.4 Performance and Optical Telescope Array | 20 |
| 11 Spitzer Space Telescope | 21 |
| 11.1 Capabilities | 21 |
| 11.2 Studies involving Spitzer | 23 |
| 12 Euclid | 23 |
| 12.1 Mission Overview | 23 |
| 12.2 Capabilities | 24 |
| 12.3 Method of Conducting Deep Survey | 24 |

| | |
|---|-----------|
| 12.4 Uses and Limitations For Euclid's Use In Studying High Redshift Galaxies | 25 |
| 12.5 Key Technical Data | 25 |
| 13 Contaminants | 25 |
| 13.1 Low Mass Stars | 25 |
| 13.2 Spurious Sources | 26 |
| 13.3 Supernovae and other transient sources | 26 |
| 13.4 Lower Redshift Sources and photometric scattering | 26 |
| Appendix | 27 |
| A Parameter Fit Data | 27 |
| References | 31 |

List of Figures

| | | |
|----|---|----|
| 1 | Diagram of a gravitational lens | 6 |
| 2 | Schematic diagram of location of images | 7 |
| 3 | The evolution of α as a function of redshift according to past observational studies. | 11 |
| 4 | The evolution of ϕ^* as a function of redshift according to past observational studies. | 12 |
| 5 | Dropout technique for model redshift 7 galaxy [1]. | 16 |
| 6 | Various filtering systems [2]. | 17 |
| 7 | Photograph of HST orbiting the Earth. | 19 |
| 8 | Diagram showing basic systems of HST, note that WFC2 has since been replaced by WFC3. | 20 |
| 9 | The Spitzer Space Telescope's Orbit [3]. | 22 |
| 10 | Number of visits required to meet the Euclid's goal of a depth of 26th magnitude. | 24 |
| 11 | The shockwave from Supernova 1987a imaged by HST in 2006. | 27 |

List of Tables

| | | |
|---|--|----|
| 1 | Data highlighting which filters would be useful for observing particular redshift galaxies [4] | 18 |
| 2 | Technical data for HST WFC3/IR camera system [5] | 21 |
| 3 | Technical data for the Spitzer orbiting telescope [5]. | 21 |
| 4 | Technical data for the Spitzer orbiting telescope [6]. | 23 |
| 5 | Euclid space telescope IR filters. | 25 |
| 6 | Technical data for the deep survey NIR photometry [7]. | 26 |

1 Introduction

1.1 Why Investigate Cosmic Re-Ionisation

There are a number of different projects in progress investigating this particular period of the universe and there are many more in the pipeline. The hydrogen re-ionization occurred due to the vast amounts of energy released when the first structures in the universe began to form. By probing this epoch we are able to study the origins of this formation and this will enable us to understand the mechanisms by which the first stars, galaxies and quasars began to form and evolve.

There are many unanswered questions in cosmology; one of the most crucial is the nature of dark energy and matter which make up around 95% of the universe [8]. These mysterious substances are thought to be the key driving force behind the evolution and expansion of the universe. By studying and mapping the distribution of Hydrogen during the EoR and tracking the evolution of stars and galaxies we are able to infer more about the effects of dark energy and what it might consist of. There are many different theories about what dark matter consist of; the current most popular theories fall under the ‘Cold Dark Matter’ model where dwarf galaxies are thought to be key building blocks in the hierarchical structure formation of the first galaxies [9].

Understanding the EoR is the missing link in explaining how the universe went from how it appears in the Cosmic Microwave Background (CMB) to what we observe today. Understanding the mechanisms of structure formation and what drives the collapse and formation of structure is fundamental in refining the concordance cosmology model. Completing the picture of what happened during the EoR will enable us to more accurately predict where the Universe is headed and how it may eventually end, will it be in a big crunch or a big freeze?

Part I

General Theory

2 Gravitational Lensing

2.1 Introduction

Contrary to a popularly held belief that Newton refers to gravitational lensing in his publication “Opticks” [10] (put into context, it is clear that he was discussing diffraction), the first person to allude directly to the bending of light due to gravitational attraction was Henry Cavendish. Around the turn of the 19th century Cavendish used Newton’s corpuscular theory to correctly calculate the bending of light around a massive object. Around the same time, German astronomer Johann Soldner was independently addressing the same problem [11] and although his results were similar to those obtained by Cavendish, his method was fundamentally flawed due to incorrect assumptions [12].

The subject of gravitational lensing was then largely put to rest until 1915 when Einstein postulated his theory of general relativity, from which it is clear that massive objects will cause light to bend as a result of the curvature of spacetime. Despite having complete and correct calculations of the phenomenon of gravitational lensing, including the lens equation and the position of images, Einstein displayed very little interest in it. He mentions it only briefly in his notebooks and published a single, very short discussion in science magazine upon the request of a friend at the end of which he dismissively comments that there is “no great chance of this phenomenon being observed” [13].

During a solar eclipse in 1919, Eddington measured the positions of stars lying close to the sun and observed that their positions appeared at a greater distance from the sun than expected, thereby giving the first experimental evidence for the bending of light around the sun [14]. 5 years later, Chwolson published a paper on the idea that ‘fake double stars’ may be observed as a result of the gravitational lensing effect and postulated that if source, lens and observer are perfectly aligned then a ‘Chwolson ring’, later renamed ‘Einstein ring’, would form around the lens [12].

The true pioneer of the subject, however, is generally considered to be Czech astronomer [15] Frantisek Link. Through detailed calculations of image magnification and positions, Link concluded that in some cases gravitational lensing would make faint sources visible. Optimistic about the possibility of observing these sources, particularly for spiral nebulae, he published a detailed paper on his wide ranging calculations which included the deflection undergone by light rays passing massive objects, the resulting change in intensity of sources and the invariance of source surface brightness. Following this, there was again a period of lack of interest, during which only a few papers were published on the subject until the discovery of the first lens in 1979 by Walsh, Carswell and Weymann. From here onwards, it became a topic of intense interest to astronomers and many more lenses and faint sources have since been discovered [12].

2.2 Concept

The bending of light around a massive object is a direct result of Einstein's theory of relativity and the curvature of spacetime. This effect can cause massive objects to act as lenses for background sources by bending the light such that rays that otherwise would not have been detected converge at the observer, resulting in a brighter image being observed. The increase in flux reaching the observer can result in significant magnification of a source, for example, one of the most distant objects known was observed behind the cluster Abell 2218 with a magnification factor of 30, equivalent to a decrease of 3.7 AB magnitudes [16]. Studying the magnification and properties of the images can yield information about both the lens and the source, making it an extremely useful tool [17]. Lensing in which multiple images are formed and the source is significantly

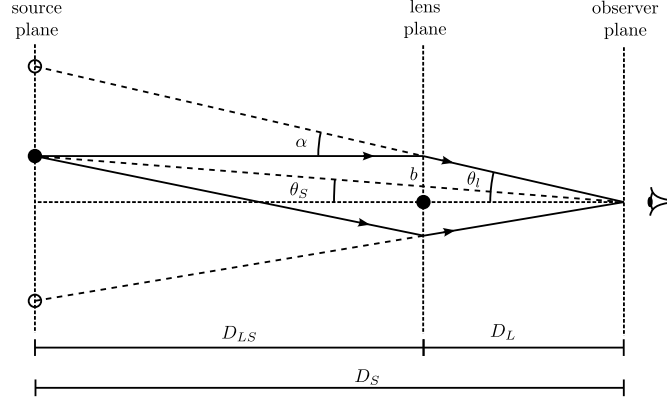


Figure 1: In this schematic diagram of a gravitational lens, D_L , D_S and D_{LS} represent the observer-lens, observer-source and lens-source distances respectively. θ_i is the image angle and θ_S the source angle, relative to the observer-lens axis. The light ray (solid line) passes by the lens at impact parameter b and as a result is deflected by angle α , converging with a second ray at the observer. The dotted lines indicate the position at which the images are observed [18].

magnified is known as strong lensing. For this to occur, the lens must have a high mass and the source angle θ_S must be small. The schematic diagram in figure 1 shows a gravitational lens acting on light from a background source in such a way as to form two images. The distances between observer, lens and source are so large in comparison to the impact parameter b that to good approximation, the lens radius is negligible and it can be modelled as a thin lens. It is therefore reasonable to assume that the light travels in straight lines at all times except in the lens plane where the complete deflection occurs. Furthermore, it can be assumed that for all values of b , the deflection angle is given by

$$\alpha = \frac{4GM}{c^2 b} \quad (2.1)$$

where M is the mass of the lens, c the speed of light and G is the gravitational constant. In realistic lensing situations, all the angles shown in figure 1 are very small, hence the small angle approximation can be applied to yield the lens equation

$$\theta_i D_S = \theta_S D_S + \alpha D_{LS} \quad (2.2)$$

and also to approximate the impact parameter to $b \approx \theta_i D_L$, it follows that

$$\theta_i = \theta_S + \frac{\theta_E^2}{\theta_i} \quad (2.3)$$

where θ_E corresponds to the Einstein angle (or Einstein radius), given by

$$\theta_E = \frac{4GM}{c^2} \frac{D_{LS}}{D_L D_S} \quad (2.4)$$

sets the characteristic angular scale for any lensing system [17].

In the rare case that the source, lens and observer in a lensing system are perfectly aligned, a ring of light is observed around the lens, known as an Einstein ring. This ring will be at a constant distance from the centre of the ring equal to the Einstein radius. More commonly, the source is offset from the observer lens axis, resulting in the formation of multiple images. The number of images formed by a lens is always odd, however, using the limit of a small but finite spherical lens, one image is formed directly behind the lens and is not observed since the lens will always be brighter.

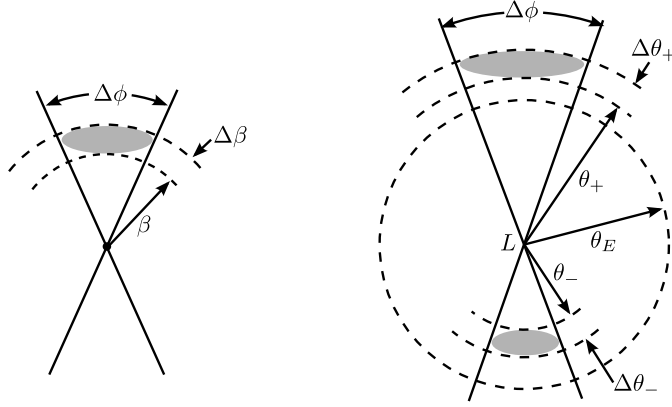


Figure 2: Schematic diagram of location of images. The centre labelled L represents the observer-lens axis. The diagram on the left shows what would be observed if the lens was not present. The right hand diagram includes the effects of lensing [17].

In the case shown in Figure lensing image positions where two visible images are observed, one image will form inside the Einstein radius (θ_{i+}) and the other outside (θ_{i-}). The positions of these two images are calculated by solving the equation 2.3 giving

$$\theta_{i\pm} = \frac{1}{2} \left(\theta_S \pm (\theta_S^2 + 4\theta_E^2)^{\frac{1}{2}} \right) \quad (2.5)$$

yielding the positions of the two images as shown in figure lensing image positions– one inside the Einstein radius, the other outside. Unlike optical lenses, gravitational lenses are achromatic, so the frequency of the light has no effect on the position of the images. As a result, images of the same object have exactly the same spectra and can easily be identified [17].

The azimuthal angle ϕ remains unchanged with and without the lens but as shown in figure lensing image positions, the polar angle and the width of the images are changed. The observed images are, therefore, stretched out into arcs and at any given radius will have the same curvature of a circle with origin at the centre of the lens [19]. The change in the polar angle θ can be calculated by differentiating equation 2.5, giving

$$\Delta\theta_{i\pm} = \frac{1}{2} \left(1 \pm \frac{\theta_S}{(\theta_S^2 + 4\theta_E^2)^{\frac{1}{2}}} \right) \Delta\theta_S \quad (2.6)$$

This shape distortion results from the fact that the sources are not point objects but in fact have light coming from a large area of the sky. The light from each end of the object will take different paths through the sky and will pass the lens at a different distance. The light will therefore be bent differently for different parts of the galaxy and the shape is distorted [20].

The magnification of the source is given by the ratio of the image brightness to the source brightness. The surface brightness of any given source remains constant [17] but the effective solid angle Ω subtended by the detector is increased by the lens, hence the flux received by the detector, given by

$$F = (\text{surface brightness}) \times \Omega \quad (2.7)$$

is also increased. Since the observed brightness of the source depends on the flux, the magnification is given by

$$\mu = \frac{F_{i\pm}}{F_S} = \frac{\Omega_{i\pm}}{\Omega_S} \quad (2.8)$$

Since in the small angle approximation, $\sin \theta \approx \theta$, the solid angles for the image and source are given by $\theta_{i\pm} \Delta\theta_{i\pm} \Delta\phi$ and $\theta_S \Delta_S \phi$ respectively. Given that $\Delta\phi$ is the same for both images, the magnification can be expressed as

$$\mu_{\pm} = \left| \left(\frac{\theta_{i\pm}}{\theta_S} \frac{d\theta_{i\pm}}{d\theta_S} \right) \right| \quad (2.9)$$

$$= \frac{1}{4} \left(\frac{\theta_S}{(\theta_S^2 + 4\theta_E^2)^{\frac{1}{2}}} + \frac{(\theta_S^2 + 4\theta_E^2)^{\frac{1}{2}}}{\theta_S} \pm 2 \right) \quad (2.10)$$

The change in AB magnitude is then found using equation 2.11 [21],

$$\Delta m = -2.5 \log(\mu) \quad (2.11)$$

The smaller the angle between the observer-lens axis and the source θ_S , the greater the magnification of the source.

Part II

Predictions

3 Predictions Group

In order for those attempting to observe high redshift galaxies to propose a detailed experimental plan, it is important to know how many galaxies one is expecting to observe within a certain volume of the sky. This is the fundamental purpose of the predictions sub-group; to be able to compute this quantity with the depth of the surveyed volume corresponding directly to redshift. In order to do this, a computer program is required to efficiently calculate this number as a function of redshift, field of view and luminosity enabling those observing to make an informed prediction of the telescope one would need and the observing time required to make definitive observation of such elusive galaxies.

This section of the project will be structured as follows:

- Research how early galaxies are professionally predicted.
- Find a general Schechter function in terms of luminosity and/or magnitude.
- Mathematically process this function to ensure it is consistent with the units used by those carrying out the observations.
- Build a computer program to automate the process of calculating the number of galaxies from the Schechter function.
- Find plausible starting parameters to use in primary program.
- Collate parameter data from published papers.
- Determine parameter evolution with time.
- Plot these results to produce a visual description of how these parameters affect the outcome.
- Give expected number of galaxies to the observers.
- Refine technique with the inclusion of more advanced adaptations

In addition to running a program to calculate the total number of galaxies, there will also be a separate program to determine the star formation rate of galaxies. This can then be used to determine an estimate of when the epoch of re-ionization occurred and hence would limit the range of redshifts which it would be necessary to include in the calculation of total number of galaxies.

4 Assumptions Made

The mathematical model that will be used in our program is limited by certain assumptions about the universe that we are working in. Some of these are generally held to be true and are accepted widely in the scientific community, others are due to the constraints of what we

can mathematically program and the observational data available from previous studies. A major assumption that we are making throughout our work on re-ionisation concerns the type of universe that we exist in. A related pair of assumptions which have firm mathematical basis are the “Cosmological Principle” and the “Isotropic Universe Theorem”. These state that our observations, as made from the Earth, are not subject to any influence from our location within it, in other words, we are not in a privileged position in the universe. This is assumed for almost all cosmological studies and shall not be considered.

An important assumption that we are forced to make is that the Schechter function that we use describes our universe sufficiently to make predictions from. This is not as trivial as it sounds since the function is derived from data collected from much lower redshifts than some that we are considering. Further data will allow the accuracy of these functions to be improved. We have collected data and mathematical contributions from a number of high redshift studies to attempt to reduce the possibility of error and increase the accuracy of our function to as high a redshift as possible.

For the early stages of our investigation, we will assume that both parameter evolution and cosmic variance do not influence the results. Clearly, these are big assumptions to make and so will be integrated into the calculations at later stages. This will be discussed further later.

5 Parameter Values

It will be assumed that the universe has a curvature of, or very close to, zero [22], in other words, that the universe is flat. This has been shown before and is generally held to be true, “we now know that the universe is flat with only a 0.4% margin of error” [23]. This means that we do not need to take into account any of the effects of observing objects near the beginning of the universe when it might have had different properties.

A second assumption that will be maintained through our calculations concerns the values of the matter, curvature and dark energy constants, Ω_M , Ω_k and Ω_Λ respectively. We will assume that we are living in a matter dominated universe and that these parameters are related to the value of the Hubble parameter by equation 5.1 [24],

$$H^2(z) = H_0^2 \left(\Omega_M(1+z)^3 + \Omega_k(1+z)^4 + \Omega_\Lambda \right) \quad (5.1)$$

where

$$\Omega_k = 1 - \Omega_M - \Omega_\Lambda \quad (5.2)$$

We will use values of $\Omega_M = 0.27$ and $\Omega_\Lambda = 0.728 \pm 0.015$, in accordance with the Λ CDM model [25].

There are also a number of parameters in the Schechter function that must be specified. In order to find suitable values to use, we collected data from a number of different sources covering several studies. All of the studies that have been performed in the past concern galaxies at lower redshifts than we are expecting to examine. To get an estimate for the value of each of the parameters at higher redshift, the values found were plotted and the fit extrapolated to cover the era necessary. Since some of the fits demonstrate that these parameters are not constant with time, their evolution shall be incorporated into the calculations.

The values in the Schechter function that we have determined fits for are α , M^* and ϕ^* . The data collected for each of these fits is shown in appendix A.

5.1 Parameter Evolution

The early stages of the models we used assumed that the parameters of the Schechter function were static with respect to time. This means that, when iterating over the redshift, the only property that changed was the co-moving volume. This is unphysical since it does not allow for changes in the characteristic mass and characteristic luminosity for different conditions in the universe. In order to improve the model, we collected data from a number of previous studies for three values, the characteristic mass, M^* , the Schechter normalisation, ϕ^* and the linear parameter, α .

5.1.1 Linear Parameter Evolution with Redshift

In order to provide useful errors on the fits of the parameters, a technique called the pivot fit method is used to decouple the errors on y -intercept and gradient. This involved fitting the data after it has been normalised around the mean value. This normalisation simply involves taking the mean x - and y -value from each data point so that the graph is centered about the origin. This means that the y -intercept is fixed to zero and thus the fitting error applies only to the gradient. Subsequent linear fits shall be treated in this manner, so that errors quoted correspond to the gradient. For clarity of presentation, the data shall be plotted in its original form.

The graph in figure 3 shows the data collected, with the corresponding uncertainties, for the linear parameter, α . From this data, a linear fit is taken.

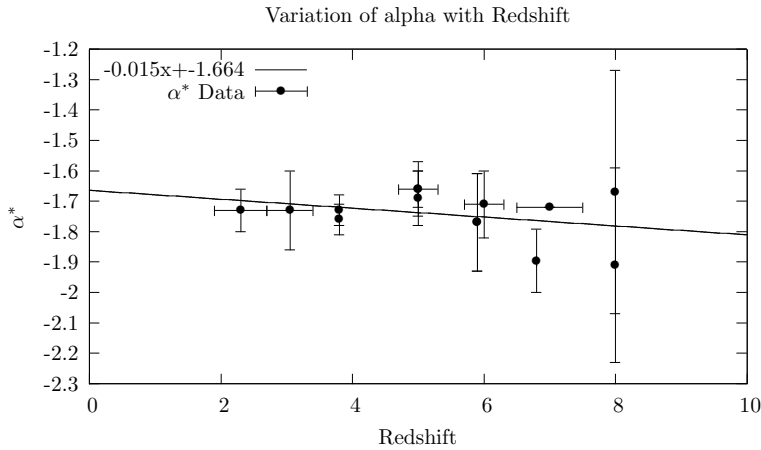


Figure 3: The evolution of α as a function of redshift according to past observational studies.

Figure 4 shows the data for the evolution of the normalisation parameter ϕ^* .

6 Cosmological Distances

This section introduces some of the important distances used in our prediction calculations. First of all is the comoving distance between two observers at different redshifts this is calculated

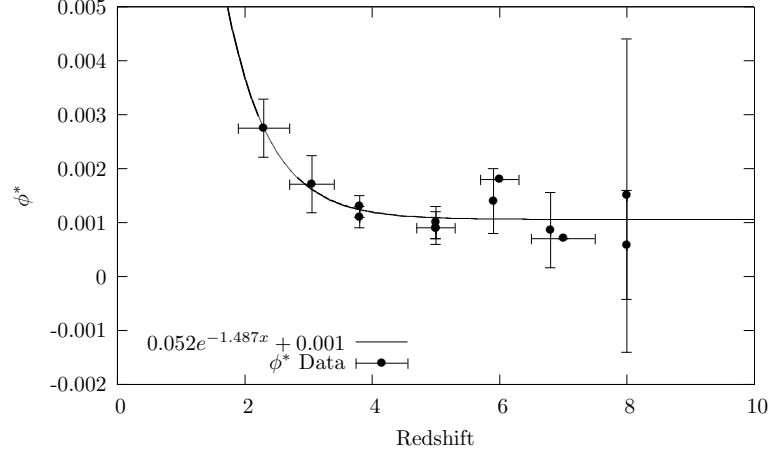


Figure 4: The evolution of ϕ^* as a function of redshift according to past observational studies.

via [26],

$$D_C(z) = \frac{c}{H_0} \int_{z_1}^{z_2} \frac{dz'}{E(z')} \quad (6.1)$$

where $E(z)$ is the dimensionless hubble parameter which general form is,

$$E(z) = \sqrt{\Omega_M(1+z)^3 + \Omega_R(1+z)^4 + \Omega_\Lambda} \quad (6.2)$$

Where the omegas are the different density parameters for mass, radiation and dark energy respectively. Therefore to calculate the comoving distance to a object at a particular redshift we use the integral above but use for $z_1 = 0$. Comoving distance is a distance between two comoving observers, i.e. factoring out the expansion of the universe. The luminosity distance is the distance a photon travels from that source. This is essentially a redshifted transverse comoving distance [26], which for a flat universe is the comoving distance therefore,

$$D_L(z) = (1+z)D_C(z) \quad (6.3)$$

This is used when converting between magnitudes, luminosity and flux.

7 Schechter Function

One important part of our project is to determine the luminosity function at high redshift, which is a plot of the number density of galaxies against their respective luminosity. A Schechter function is used to fit this luminosity function. A Schechter function is a form that has a power law which at a certain cut-off at which it becomes an exponential curve. The Schechter function in terms of luminosity, i.e. the luminosity function is shown below [27].

$$\phi(L) = \phi^* \left(\frac{L}{L^*} \right)^\alpha e^{-L/L^*} \quad (7.1)$$

The three parameters, ϕ^* , L^* and α , in our project, are cited from various sources at different redshifts. ϕ^* is the normalisation factor in units of Mpc^{-3} , α is the gradient of the faint end slope of the luminosity function and L^* is the characteristic luminosity at which the function changes from a power law to an exponential cut off.

There are two basic methods to determine the best fit parameters of the Schechter function [28]. The first one is to take cluster samples and bin them by apparent magnitude then fit a Schechter function trying to minimise the error. The other way is to use the “maximum likelihood method”. This method takes a flux limited sample and finds the probability that a galaxy actually has a particular luminosity at respective distances and then define a likelihood function which is the joint probability of finding all luminosities at their respective distances. These are then the most likely parameters consistent with the data and a Schechter form. Although we simply used Schechter parameters from articles in our project.

The luminosity function can then be integrated to find the number density in Mpc^{-3} ,

$$\rho_N = \int_L^\infty \phi(L) dL \quad (7.2)$$

Where L is the lower limit luminosity that can be seen in the universe, this is needed as the luminosity function tends to infinity at the faint end.
or luminosity density of galaxies in $\text{erg s}^{-1} \text{Mpc}^{-3} \text{Hz}^{-1}$.

$$\rho_L = \int_L^\infty L \phi(L) dL \quad (7.3)$$

A Schechter function is also used for the mass function of dark matter halos, this suggests a relation between the dark matter halo mass and luminosity of their galaxies. However it turns out that this is not an exact relation due to feedback and baryonic cooling.

7.1 Number of Galaxies

To get a lower limit luminosity for the integral of the number density integral, we can use the jeans mass at a particular redshift and for a given mass to light ratio. However this will be very much a lower limit as we are unlikely to actually see galaxies at jeans mass, or they may not actually form due to supernovae and AGN feedback. It is easier to plot the luminosity function on the log scale and therefore most of the papers we cite state the absolute magnitude Schechter function instead which is,

$$\phi(M) = \phi^* (\ln 10) \left(10^{0.4(M^* - M)} \right)^{\alpha+1} \exp \left(-10^{0.4(M^* - M)} \right), \quad (7.4)$$

where M^* is the characteristic absolute magnitude where the cut off happens. However the observing team will be looking at a range of apparent magnitudes rather than absolute magnitudes and so we can change the absolute magnitude equation above to apparent using the simple relationship below,

$$m = M + 5((\log_{10} D_L) - 1), \quad (7.5)$$

where D_L is the luminosity distance.

7.2 Star Formation Rate

Star formation rate is directly related to luminosity via the relationship in equation 7.6 [29],

$$\text{SFR}(M_{\odot}\text{yr}^{-1}) = 1.4 \times 10^{-28} L_{\nu}(\text{erg s}^{-1} \text{Hz}^{-1}) \quad (7.6)$$

Therefore we can get a star formation rate density from the luminosity density calculated from our Schechter function. This is useful to us as it will let us calculate the rate of ionizing photons in the high redshift universe via the equation,

$$\frac{dn_{\text{ion}}}{dt} = f_{\text{esc}} \zeta \rho_{\text{SFR}} \quad (7.7)$$

Part III

Observations

8 Observing Strategy Group

This primary aim of this subgroup is to formulate an observing strategy capable of probing the depths of the Epoch of Reionization. Our strategy is going to be based upon using optical techniques to detect candidate Lyman Break Galaxies (LBG) and confirming their properties using spectroscopy.

The study of this era in the universe's history has come a long way in the past 30 years and with the selection of new telescopes and radio arrays being designed currently it is only set to accelerate over the coming decades. It is a massive understatement to say such distant redshifts are very difficult to see and it is a testament to scientific and engineering achievement that we are able to take the detailed images we can. The light from these galaxies is so faint that it can take a very long time to see anything. Due to this lengthy nature of the projects, time on telescopes is highly sought after and very competitive.

This strategy must therefore be as complete as possible with as many influencing factors included. This strategy will have two main focuses:

- Using the most efficient methods available in order to limit the observing time required.
- To probe the beginning of Reionization; there have been few observations above $z = 10$ and future telescopes will have the ability to break new frontiers and observe what happened at these earliest moments of structure formation.

Our strategy will look to utilise the capabilities of the new technology to further the scientific understanding of the EoR.

The observing strategy will be established as follows:

- Research possible telescopes capable of observing high-redshift objects.
- Explore the advantages and disadvantages of ground and space-based telescopes.
- Identify the most efficient telescope for a wide survey of the sky to locate candidates; this will be determined using exposure time calculations.
- Research gravitational lensing, its possible application in assisting our wide surveys and how we might locate more lenses.
- Identify the telescope which will produce the highest resolution imaging of in a narrower deep survey; this will be established using exposure time calculations and observational limits of the system.
- Identify a telescope capable of spectroscopically confirming the nature and redshift of the candidates.
- Investigate the application of methods such as colour-colour diagrams for selecting candidates and removing contaminants from the sample.

- Compile a ‘Final Observing Strategy’ capable of observing the EoR using numerical predictions from the predictions subgroup.

This ‘Final Observing Strategy’ will give calculations of the observation time required (inc. photometry, overheads, spectroscopy), the timescale on which the project can be actioned, the limitations of our strategy, possible areas for optimisation/refinement and areas for further research.

9 Determining Redshift

Need a section on candidates and how the contaminants are eliminated. (COMBINE WITH JOE’S COLOUR STUFF?)

Section ?? described how contaminants could be eliminated from the large number of potential high redshift galaxies. Taking the remaining objects, the following methods are used to check whether they are in fact LBGs.

9.1 Filters and the Dropout Technique

Using photometry, the redshift of a LBG can be estimated using the dropout technique: The flux from the galaxy can be measured in three different bands, ideally two above and one below the Lyman break. If the galaxy is a high redshift Lyman break galaxy, it would be expected that, so long as the filters were correct for the redshift expected, one image would not see the galaxy whereas the other two would observe flux. Below in figure 5, the dropout technique is shown for a model galaxy of redshift seven.

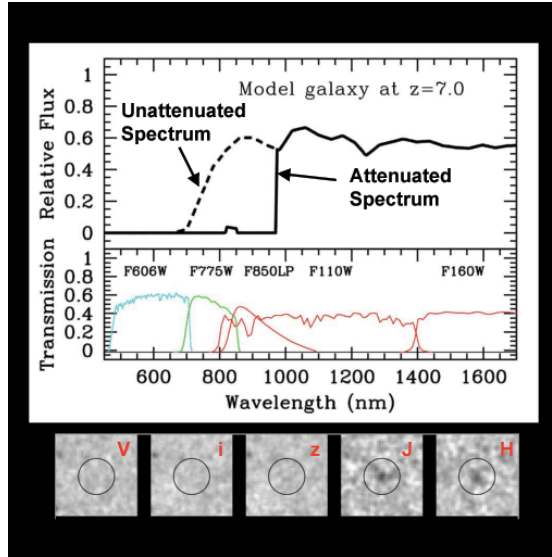


Figure 5: *Dropout technique for model redshift 7 galaxy [1].*

The neutral hydrogen has attenuated almost all flux at wavelengths shorter than approximately

1 micrometre. The galaxy has been imaged in several different bands, and the longer wavelength filters show flux, whereas those at wavelengths corresponding to blue-ward of Lyman alpha do not. The galaxies that the group look to study have been shifted such that the drop happens in the infra-red. The wavelength of the drop can be worked out using the known rest wavelength of Lyman alpha, as well as the factor by which the wavelength shifts due to the expansion of the universe, as shown in equation 9.1.

$$\text{Rest wavelength of Lyman alpha} \times (1 + z) = \text{observed wavelength of drop} \quad (9.1)$$

Since the rest wavelength of Lyman alpha is known and the observed wavelength of the drop can be measured, the redshift of the galaxy can be determined. This is only a rough estimate when doing photometry since the flux is simply a number in each of the bands. For example, if the bands do not overlap, and the drop happens between two bands, it will not be known at what point the drop occurred, only the range in which it occurred. This motivates the use of bands which are close together or potentially even overlapping. Figure 6 shows some different bands and their bandwidth, for different filter systems. Johnson-Cousins- Glass is one of the oldest and still the most commonly used system [30].

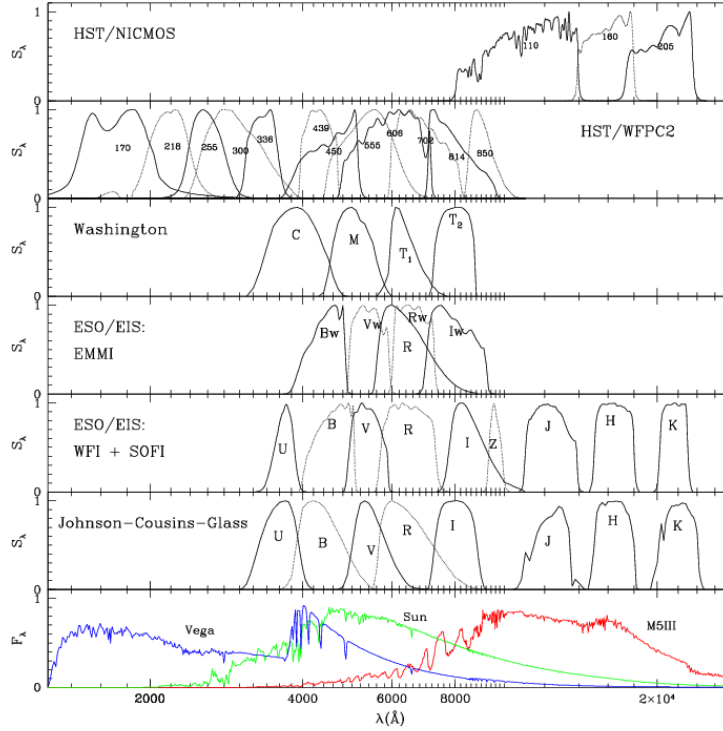


Figure 6: Various filtering systems [2].

The bandwidth (or passband) is the wavelength range that can pass through the filter. Filters in different parts of the spectrum are given a common name, for example I band at 806 nanometres. When observing LBGs, it is beneficial to have three filters in a row so that the position of the drop can be more accurately measured. As can be seen, there are gaps between the J H and K filters, meaning if the drop occurs between J and H, full flux should be observed in H and K

and virtually no flux should be seen in J. (the panels beneath figure 6 show an image (or lack thereof) of the $z=7$ galaxy in each of the V, I, z, J and H bands)

Table 1 below shows a list of filter names, the central wavelength of that filter, the bandwidth the filter covers, and range of redshifts for which the Lyman alpha drop would be covered. (This range assumes the bandwidth covers 50% either side of the central wavelength)

| Filter | Central wavelength | Bandwidth | Redshift coverage |
|--------|--------------------|-----------|-------------------|
| V | 551 nm | 88 nm | 3.17–3.90 |
| i | 806 nm | 149 nm | 5.01–7.25 |
| Y | 1020 nm | 120 nm | 6.90–7.88 |
| J | 1220 nm | 213 nm | 9.16–9.91 |
| H | 1630 nm | 307 nm | 11.14–13.67 |
| K | 2190 nm | 390 nm | 15.41–18.61 |

Table 1: *Data highlighting which filters would be useful for observing particular redshift galaxies [4]*

Table 1 must be taken into consideration that two filters should be red-ward of the drop and one blue-ward. One the fluxes have been measured in all three bands, if the object is indeed a LBG, there should be a sharp drop in flux in one of the bands. However this does not totally rule out other possibilities: Some other objects could also exhibit a drop in flux, posing as LBGs, so usually a follow up method is used, and this is spectroscopy. Spectroscopy The drop out technique provides a good indication that a galaxy is a high redshift Lyman break galaxy, however the best way to confirm this is with spectroscopy. Spectroscopy involves...

At loads of different wavelengths, measure the spectra. Look for the drop

Use ground based such as KECK or space based, JWST will have one.

10 The Hubble Space Telescope

10.1 Mission Launch

On April 24th 1990 NASA's Space Shuttle Discovery launched the world's first space-based optical telescope; The Hubble Space Telescope (HST), named in honour of American astronomer Edwin P. Hubble. Edwin Hubble's greatest contribution to astronomy was the Hubble Law which states that galaxies are receding from us at a speed directly proportional to their distance from us. This showed that our universe is expanding, a notion which underpins modern cosmological thinking. The telescope sits in a low-Earth orbit, as shown in figure 7, at an altitude of 569 kilometres completing one orbit of the Earth every 97 minutes [31].

The HST was designed to provide clear and deep views of distant galaxies and stars and most of the planets in our solar system. Hubble's domain extends from the ultraviolet through the visible and into the near-infrared [32].



Figure 7: *Photograph of HST orbiting the Earth.*

10.2 Achievements to Date

The HST has provided unprecedented detail in images of star formation allowing astronomers to see the jets and disks present during the birth of new stars. It has also been able to study the atmospheric composition of extra-solar planets and take the first visible light picture of a planet outside our solar system; Fomalhaut b [33].

Many EoR galaxies and candidate galaxies have been identified using HST data. In December 1995 the HST was pointed at what was believed to be a fairly empty and uninteresting patch of sky; 342 separate exposures were taken over 10 consecutive days and formed an image called the Hubble Deep Field (HDF) [34]. The image contains around 3,000 objects of which the vast majority are galaxies, with a few local stars in the foreground. The HDF is one of the most iconic images of the 20th century, and it has since been cited in over 800 scientific papers.

In 2004 its successor was revealed, the Hubble Ultra Deep Field (UDF); a million-second exposure in a $200'' \times 200''$ area of sky containing 10 000 galaxies stretching back 13 billion years [35]. This exposure utilised the recently installed Advanced Camera for Surveys (ACS). This survey was further refined in September 2012 in the Hubble eXtreme Deep Field (XDF) which utilised the recently installed WFC3 camera as well as combining over 2000 separate exposures from different sources [34].

Using data from the HUDF, object UDFj-39546284 was identified. In a paper by Bouwens et al, published in 2012, their best fit places it at a redshift of 11.8 ± 0.3 [36]. This would classify it as the oldest object ever observed. The exact nature of the object is not known but it is believed to be a mini-galaxy. Confirmation will require spectroscopic analysis, which is likely to be carried out by the James Webb Space Telescope. This observation demonstrates both the achievements and limits of the current technology.

10.3 Operation

The HST is operated remotely from the earth, it has 4 antennae which can send and receive signals from the Flight Operations Team at Goddard Space Flight Centre in Greenbelt, Maryland via

the Tracking and Data Relay Satellite system. For communication to be possible HST must have a direct line of sight to at least one of these 5 satellites.

The HST is powered using 2 arrays of solar panels each capable of converting the Sun's rays into 2800 watts of electricity. The arrays are able to store the electricity in batteries allowing the HST to remain active while in the Earth's shadow (approximately 36 minutes out of every 97 minute orbit).

Orbiting the Earth subjects the HST to extreme conditions due to the effect of zero gravity and the variation in temperature (up to around 40 K) during each orbit. The optical system is held together using a skeleton (truss) constructed from Graphite epoxy. Graphite epoxy, commonly found in racquets and golf clubs is a stiff and lightweight material able to resist expansion and contraction due to temperature changes [37].

10.4 Performance and Optical Telescope Array

The HST is constructed using a Ritchey-Chretien Cassegrain design; this allows high-performance over a wide field of view. The incoming light enters a tube with baffles removing any unwanted stray light, as shown in figure 8 below. The light is then collected by the concave Primary mirror and reflected towards the smaller convex Secondary mirror. This light is then reflected back through a hole in the centre of the Primary mirror where it is focused onto a small area to be picked up by the instruments [38].

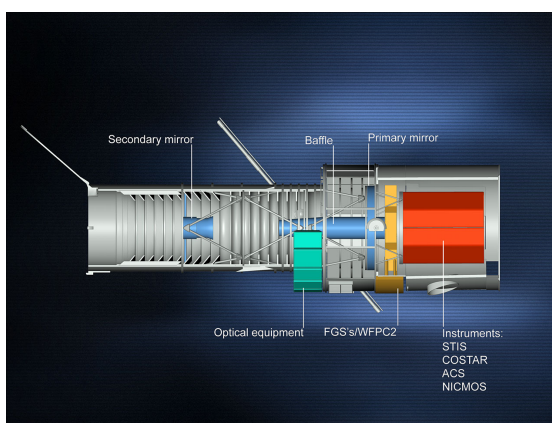


Figure 8: Diagram showing basic systems of HST, note that WFC2 has since been replaced by WFC3.

The mirrors have been polished to an accuracy of better than the wavelength of visible light. When the HST was first launched the scientists soon realised that the curve to which the mirrors had been ground was not correct resulting in an error known as spherical aberration which blurred the images. A servicing mission in December 1993 deployed 5 pairs of mirrors which were able to successfully correct the error and allow Hubble to take the images it was intended to [39].

There have been 4 servicing missions sent to the HST with the final mission taking place in May 2009. Over its lifetime the cameras and instruments have undergone many improvements and replacements. The camera currently operating that is of interest to this project is the WFC3/IR

camera, installed in 2009. This camera is able to observe in the near-infra-red where we expect to see the Lyman-break galaxies. Table 2 shows the key technical data for the HST, amazingly the HST is so precise it is able to lock onto a target at a distance of 1 mile without deviating more than the width of a human hair.

| Component | Details |
|---------------------------|--|
| Primary Mirror Diameter | 2.4 m |
| Secondary Mirror Diameter | 0.3 m |
| Wavelength range | 800–1700nm |
| Total Field of View | $123'' \times 136''$ ($16\,728''^2$) |
| Pixel Size | $18 \times 18\,\mu\text{m}$ |
| Plate Scale | $0.13''\,\text{pix}^{-1}$ |
| Quantum Efficiency | 77% at 1000 nm 79% at 1400 nm 79% at 1650 nm |
| Dark count | $0.048\,\text{e}^- \text{s}^{-1}\,\text{pix}^{-1}$ |
| Readout noise | $12.0\,\text{e}^- \text{s}^{-1}\,\text{pix}^{-1}$ |
| Full Well | $77\,900\,\text{e}^-$ |
| Gain | $2.28\text{--}2.47\,\text{e}^- \text{ADU}^{-1}$ |
| Operating Temperature | 145 K |
| FWHM | $0.151'$ at 1600 nm |

Table 2: *Technical data for HST WFC3/IR camera system [5]*

11 Spitzer Space Telescope

Spitzer Space telescope was launched by NASA on 25th August 2003 [40] and is designed for use in the infra-red. It was the last of NASA’s “Great Observatories”, working alongside HST in the optical, Compton Gamma Ray Observatory and Chandra X-ray Observatory. The telescope is 85 cm in diameter, and sits in an Earth-trailing orbit around the Sun, shown in figure 9. It is a Cassegrain telescope, meaning it has primary and secondary hyperbolic mirrors to focus the light and reduce spherical aberration, in a similar manner to Hubble. The majority of Spitzer’s instrumentation is now non-operational due to a lack of cryogen, but some photometry remains possible.

11.1 Capabilities

Spitzer had the capabilities detailed in table 3:

| Component | Details |
|--------------------|----------------------|
| Imaging/Photometry | 3–180 μm |
| Spectroscopy | 5–40 μm |
| Spectrophotometry | 50–100 μm |

Table 3: *Technical data for the Spitzer orbiting telescope [5].*

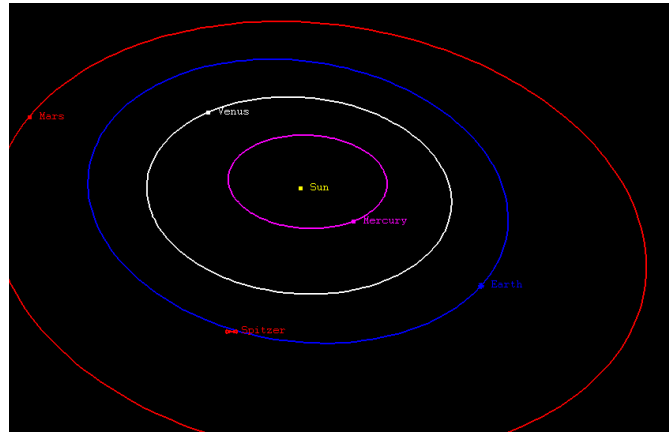


Figure 9: *The Spitzer Space Telescope's Orbit [3].*

It employed three scientific instruments which helped it do the above:

- Infrared Array Camera (IRAC): an imaging camera working in the near IR at wavelengths of 3.6, 4.5, 5.8 and 8 micrometres.
- Infrared Spectrograph (IRS): performing spectroscopy from 5 to 40 micrometres.
- Multiband Imaging Photometer (MIPS): detected wavelengths in the far IR, at 24, 70 and 160 micrometres.

The telescope was cryogenically cooled to around 1.4 K, allowing all the instruments to function without excessive thermal interference from the telescope itself. The mission, labelled the 'Cold Mission', was estimated to last between 2 and 5 years, depending on when the cryogen ran out. During this time, Spitzer imaged in all four NIR filters simultaneously, as well as doing spectroscopy, and some imaging in the far infra-red. In 2009, when the cryogen ran out, the longer wavelength filters became non-operational, and the Spitzer 'Warm Mission' continued imaging with the nearest IR filters (3.6 and 4.5 micrometres). This was made possible because Spitzer's orbit keeps it substantially cooler than an Earth-centred orbit would, due to the lack of IR radiation received from Earth. Furthermore it is made mostly of beryllium which has a low heat capacity at low temperatures, helping to keep it cool.

In order to keep enough sunlight on the solar panels, Spitzer cannot point further than 120 degrees away from the Sun. However, it also cannot get closer than 80 degrees towards the Sun in case damage is done to the scientific instruments. This is a limitation on the area of sky which can be observed, meaning that some regions can only be seen for 40 days semi-annually, whilst other areas can be observed all year round.

The spectrograph (IRS) operated at wavelengths too long to be of use to study the EoR, as did the far IR photometry (MIPS), however the near IR photometry capabilities of both the Spitzer warm and cold missions have been used to study high redshift galaxies, and in conjunction with HST have confirmed galaxies at redshifts as far back as $z \approx 10$. Particularly the 3.6 and 4.5 micrometre filters observe significant flux from such galaxies, and so these have been used in a number of studies looking for high redshift galaxies.

11.2 Studies involving Spitzer

Coe et al (2012) [41] reports a $z \approx 11$ candidate which had been observed using HST (WFC3, ACS) and Spitzer (IRAC) for longer wavelengths. This is one of the highest redshift candidates to date. The Spitzer data was taken over a total integration time of 5 hours.

An earlier study in 2008 by Richard et al also used Hubble to detect galaxies greater than redshift seven (making use of gravitational lenses). Spitzer imaged these galaxies to help confirm that they were not foreground objects of a different nature, by looking at the flux in longer wavelength filters [42].

In 2005, during the cold mission, a study was made by Spitzer on a confirmed $z = 6.56$ galaxy (HCM 6A) lensed by a cluster (Abell 370). The study was used to detect the rest frame optical emission of this galaxy in order to better understand the physical properties of objects at such high redshifts [43]. Several other papers have also used Spitzer data in the study of high redshift galaxies.

The data in table 4 shows some of the key technical data available for the telescope.

| Component | Details |
|----------------|------------------------------|
| Primary mirror | 0.85 m |
| FoV | $5.2' \times 5.2'$ |
| Pixel size | $1.2'' \times 1.2''$ |
| Detector Array | 256×256 pix |
| Full well | 145,000 at $3.6 \mu\text{m}$ |
| | 140,000 at $4.5 \mu\text{m}$ |

Table 4: Technical data for the Spitzer orbiting telescope [6].

12 Euclid

12.1 Mission Overview

The Euclid mission is planned for launch in 2018 [7, p. 8] at an estimated total cost of 800 million Euros, and will work in the optical and near infra-red [44]. Its primary goal is to conduct a wide survey, some 15000 degrees of sky is planned to be covered, in order to map the geometry of the dark universe. It will look at galaxies and galaxy clusters to work out their red-shifts and shapes, back to $z = 2$. There is also to be a deep survey which is expected to cover around 40 degrees of sky to a depth 2 magnitudes deeper than the wide survey. This deep survey will allow astronomers to see even further back in time, up to red-shifts of 8 and potentially even higher. The primary mission objectives are expected to be completed within 7 years.

One of Euclid's main scientific objectives with the deep survey is to study high red-shift galaxies at $z \geq 6$ over a very wide survey area. This will give astronomers the opportunity to spectroscopically confirm hundreds of galaxies for use in the study of the EoR. It will help constrain the bright end of the luminosity function at high z . Euclid will "detect hundreds of $z = 7$ galaxies brighter than an apparent magnitude $J = 26$ and tens at z greater than 8" [7].

Another is to study clusters of galaxies in the near IR as well as the visible; a weak gravitational lensing survey (as discussed in section ?? Grav lensing by Catherine) will be carried out, looking for disturbances and distortions in the light from galaxies as a result of large amounts of mass perturbing the path of the photons emitted from them. “Euclid measures the shapes of 30 resolved galaxies per arcmin² in one broad visible R+I+Z band (550–920 nm) down to AB mag 24.5” [7, p. 9].

12.2 Capabilities

- Visual Imaging/ Photometry, 550–900nm
- Spectroscopy, 1100–2000nm
- NIR Imaging/ Photometry, 920–2000nm (Y, J,H bands)

Euclid will have two instruments in order to do the above; a wide-band imaging system in the visible (VIS), and an instrument capable of both slit-less spectroscopy as well as NIR imaging (NISIP). These instruments will be able to operate simultaneously when required.

12.3 Method of Conducting Deep Survey

The Euclid deep survey will be carried out by re-visiting particular areas in the wide survey over an extended period of time. Over this time, the depth will be built up by combining a series of images taken of the same piece of sky (known as stacking). The wide survey will reach the required magnitude depth with one exposure, but to reach 2 magnitudes deeper (26th magnitude AB at 5 sigma) considerably more exposures will be needed. Figure 10 shows the number of visits to increase the depth to 26th magnitude. The current estimate is that this will take around 36 exposures, and it has been decided to do 40 to make sure [45]. The telescope operates a 4 step dithering mode so that if there are faulty pixels or systematic errors, the image is still usable.

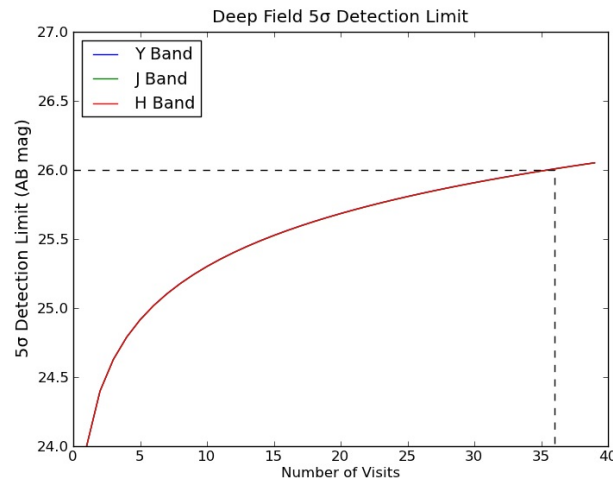


Figure 10: Number of visits required to meet the Euclid’s goal of a depth of 26th magnitude.

12.4 Uses and Limitations For Euclid's Use In Studying High Redshift Galaxies

The main limitation of using Euclid for this study is its filter range: Since the drop out technique requires two filters above the drop and one below, the red-shift of the galaxy must be such that the filters available are able to achieve this. Euclid's longest wavelength filter is centred at $1.63\mu\text{m}$ (J-band filter). If the drop is at too long a wavelength, only one band will observe flux. Without two bands observing flux, no colour-colour diagrams can be plotted, and one measurement of flux and another of no flux is not enough to have confidence that the object is a Lyman break galaxy. Table 5 shows the IR filters of Euclid, along with each filter's central wavelength and it's bandwidth.

| Filter | Central Wavelength | Bandwidth |
|---------------|--------------------|-----------|
| Y (920–1146) | 1020 | 226 |
| H (1146–1372) | 1220 | 226 |
| J (1372–2000) | 1630 | 628 |

Table 5: *Euclid space telescope IR filters.*

From this, it can be concluded that the survey will be unhelpful in determining galaxies past a red-shift of 10.5 (corresponding to the drop being observed at $1.40\mu\text{m}$): The object would be detected in the J band, but not in either H or Y. The end of the H filter and start of the J filter is at $1.37\mu\text{m}$. To get significant flux in the Y band, ideally the galaxy would need to be at a red-shift of 10 or lower, such that a noticeable amount of flux was detected in H.

A weak lensing survey is planned with Euclid. This will help find gravitational lenses which could be used to magnify very faint Lyman break galaxies at high red-shift. From this weak lensing survey, the strongest lenses could be selected and used as targets for other telescopes such as JWST or ELT to study more closely to see if any high red-shift LBGs lay behind.

The spectroscopic mode can be used (grism spectroscopy) to determine the red-shift of LBGs as outlined in section ???. The advantage of grism spectroscopy is that multiple objects can be studied simultaneously, meaning if there are multiple likely candidates in the field of view, their spectra can all be gathered at once, reducing the overall time taken to study a large number of red-shift galaxies. This is particularly useful to Euclid, which has a wide field of view of just over 0.5 square degrees, increasing the chance of multiple candidates.

12.5 Key Technical Data

The data in table 6 is quoted for the deep survey NIR photometry. Some data is subject to slight change as the planning stages progress.

13 Contaminants

13.1 Low Mass Stars

These can easily be identified due to the high resolution imaging provided by The Point-spread function (PSF) obtained will allow us to determine which sources are point-like and which

| Component | Details |
|-------------------------|--------------------------------|
| Primary mirror | 1.2 m |
| FoV | $0.763 \times 0.763^{\circ 2}$ |
| Pixel size | $0.3'' \times 0.3''$ |
| Detector Array | 2000×2000 pix |
| Resolution | 0.3 to $0.6''$ (in J band) |
| Plate Scale (infra-red) | $0.3'' \text{ pix}^{-1}$ |

Table 6: *Technical data for the deep survey NIR photometry [7].*

are extended. We should be able to avoid significant contamination by removing any point-like sources from the results as all galaxies should have a great enough diameter.

13.2 Spurious Sources

By stipulating that we will be requiring detections in two bands the influence of spurious sources will be negligible. Finding detections in 2 bands at reasonable confidence interval (?3sig?) is very improbable. By inspecting the negative with the same requirements for detection we are able to identify any such sources easily [46].

13.3 Supernovae and other transient sources

Events such as Supernovae happen incredibly quickly releasing a vast amount of energy, as seen in figure 11. These events can spoil images due to their short duration by introducing new data in only a portion of the sample. These effects are usually only considered when taking exposures years apart or when combining multiple sources over a long timescale. Such events are very unlikely to contaminate our results as we propose to take our images close in time.

13.4 Lower Redshift Sources and photometric scattering

This category is likely to provide the greatest source of contamination for the surveyed area. It will do so increasingly at high redshifts where its affect on the faintest magnitudes is most greatly felt. Its affect is most influential with a small S/N ratio for the observations, by fixing this at a level of $S/N = \dots$ we can be confident that the contamination will be low. Detecting a source in another band such as b435, v606, i775 for YJH photometry would class it as a contaminant and then should be removed from sample.

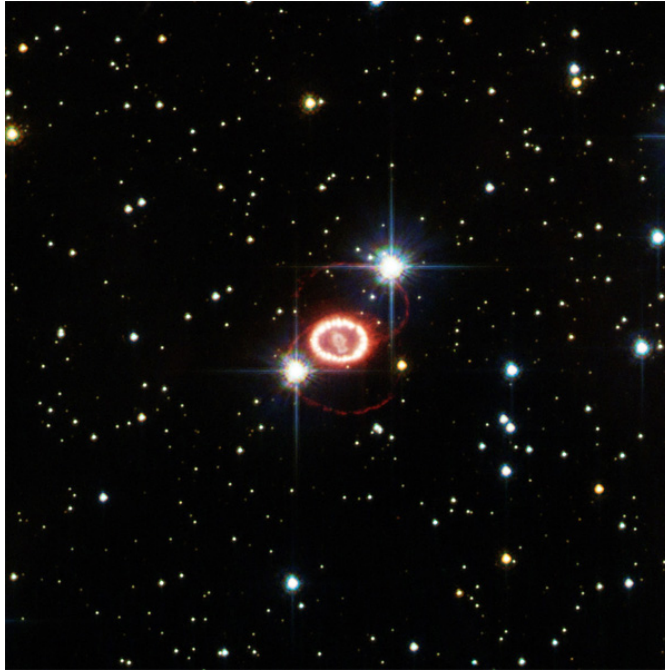


Figure 11: *The shockwave from Supernova 1987a imaged by HST in 2006.*

A Parameter Fit Data

References

- [1] G. Illingworth. A resource for research on the most distant galaxies. <http://www.firstgalaxies.org/the-first-galaxies>, 2011.
- [2] L. Girardi, G. Bertelli, A. Bressan, C. Chiosi, M. A. T. Groenewegen, P. Marigo, B. Salasnich, and A. Weiss. Theoretical isochrones in several photometric systems. *A&A*, 391(1):195–212, 2002.
- [3] NASA/JPL-Caltech. Where is spitzer now? http://www.spitzer.caltech.edu/mission/where_is_spitzer, 2013.
- [4] J. Binney and M. Merrifield. *Galactic Astronomy*. Princeton University Press, 1998.
- [5] L. Dressel. *Wide Field Camera 3 Instrument Handbook, Version 5.0*. StScI, Baltimore, 2012.
- [6] IRAC Instrument and Instrument Support Teams. Spitzer: Data archive. <http://sha.ipac.caltech.edu/applications/Spitzer/SHA/>, 2013.
- [7] R. Laureijs, J. Amiaux, S. Arduini, J. -L. Auguères, J. Brinchmann, R. Cole, M. Cropper, C. Dabin, L. Duvet, A. Ealet, B. Garilli, P. Gondoin, L. Guzzo, J. Hoar, H. Hoekstra, R. Holmes, T. Kitching, T. Maciaszek, Y. Mellier, F. Pasian, W. Percival, J. Rhodes, G. Saavedra Criado, M. Sauvage, R. Scaramella, L. Valenziano, S. Warren, R. Bender, F. Castander, A. Cimatti, O. Le Fèvre, H. Kurki-Suonio, M. Levi, P. Lilje, G. Meylan, R. Nichol, K. Pedersen, V. Popa, R. Rebolo Lopez, H. -W. Rix, H. Rottgering, W. Zeilinger, F. Grupp, P. Hudelot, R. Massey, M. Meneghetti, L. Miller, S. Paltani, S. Paulin-Henriksson, S. Pires, C. Saxton, T. Schrabback, G. Seidel, J. Walsh, N. Aghanim, L. Amendola, J. Bartlett, C. Baccigalupi, J. -P. Beaulieu, K. Benabed, J. -G. Cuby, D. Elbaz, P. Fosalba, G. Gavazzi, A. Helmi, I. Hook, M. Irwin, J. -P. Kneib, M. Kunz, F. Mannucci, L. Moscardini, C. Tao, R. Teyssier, J. Weller, G. Zamorani, M. zapatero osorio, O. Boulade, J. foumond, A. Di Giorgio, P. Guttridge, A. James, M. Kemp, J. Martignac, A. Spencer, D. Walton, T. Blümchen, C. Bonoli, F. Bortoletto, C. Cerna, L. Corcione, C. Fabron, K. Jahnke, S. Ligorì, F. Madrid, L. Martin, G. Morgante, T. Pamplona, E. Prieto, M. Riva, R. Toledo, M. Trifoglio, F. Zerbi, F. Abdalla, M. Douspis, C. Grenet, S. Borgani, R. Bouwens, F. Courbin, J. -M. Delouis, P. Dubath, A. Fontana, M. Frailis, A. Grazian, J. Koppenhöfer, O. Mansutti, M. Melchior, M. Mignoli, J. Mohr, C. Neissner, K. Noddle, M. Poncet, M. Scodeggio, S. Serrano, N. Shane, J. -L. Starck, C. Surace, A. Taylor, G. Verdoes-Kleijn, C. Vuerli, O. williams, A. Zacchei, B. Altieri, I. Escudero Sanz, R. Kohley, T. Oosterbroek, P. Astier, D. Bacon, S. Bardelli, C. Baugh, F. Bellagamba, C. Benoist, D. Bianchi, A. Biviano, E. Branchini, C. Carbone, V. Cardone, D. Clements, S. Colombi, C. Conselice, G. Cresci, N. Deacon, J. Dunlop, C. Fedeli, F. Fontanot, P. Franzetti, C. Giocoli, J. Garcia-Bellido, J. Gow, A. Heavens, P. Hewett, C. Heymans, A. Holland, Z. Huang, O. Ilbert, B. Joachimi, E. Jennins, E. Kerins, A. Kiessling, D. Kirk, R. Kotak, O. Krause, O. Lahav, F. van Leeuwen, J. Lesgourgues, M. Lombardi, M. Magliocchetti, K. Maguire, E. Majerotto, R. Maoli, F. Marulli, S. Maurogordato, H. McCracken, R. McLure, A. Melchiorri, A. Merson, M. Moresco, M. Nonino, P. Norberg, J. Peacock, R. Pello, M. Penny, V. Pettorino, C. Di Porto, L. Pozzetti, C. Quercellini, M. Radovich, A. Rassat, N. Roche, S. Ronayette, E. Rossetti, B. Sartoris, P. Schneider, E. Semboloni, S. Serjeant, F. Simpson, C. Skordis, G. Smadja, S. Smartt, P. Spano, S. Spiro, M. Sullivan, A. Tilquin, R. Trotta, L. Verde, Y. Wang, G. Williger, G. Zhao, J. Zoubian, and E. Zucca. Euclid definition study report. *ESA report*, 2011.

- [8] G. Hinshaw, D. Larson, E. Komatsu, D. N. Spergel, C. L. Bennett, J. Dunkley, M. R. Nolta, M. Halpern, R. S. Hill, N. Odegard, L. Page, K. M. Smith, J. L. Weiland, B. Gold, N. Jarosik, A. Kogut, M. Limon, S. S. Meyer, G. S. Tucker, E. Wollack, and E. L. Wright. Nine-Year Wilkinson Microwave Anisotropy Probe (WMAP) Observations: Cosmological Parameter Results. *ArXiv e-prints*, December 2012.
- [9] M. Cignoni and M. Tosi. Star Formation Histories of Dwarf Galaxies from the Colour-Magnitude Diagrams of Their Resolved Stellar Populations. *Advances in Astronomy*, 2010, 2010.
- [10] Isaac Newton. *Opticks: or, a treatise of the reflections, refractions, inflections and colours of light. Fourth Edition.* 1730.
- [11] Joachim Wambsganss. Gravitational lensing in astronomy. *Living Reviews in Relativity*, 1(12), 1998.
- [12] David Valls-Gabaud. The conceptual origins of gravitational lensing. *Albert Einstein Century International Conference, AIP Conference Proceedings*, 861:1163–1171, Jun 2006.
- [13] Albert Einstein. Lens-like action of a star by the deviation of light in the gravitational field. *Science. New Series*, 84:506–507, Dec 1936.
- [14] Bernard Burchell. General Relativity Experiments. <http://www.alternativephysics.org/book/GRexperiments.htm>, 2011.
- [15] Jiří Bičák. Einstein’s Days and Works in Prague. http://ae100prg.mff.cuni.cz/presentations/Bicak_Jiri.pdf, 2012.
- [16] C.R. Nave. Magnification with a Gravitational Lens? <http://hyperphysics.phy-astr.gsu.edu/%E2%80%8Chbase/Astro/glens.html>, 2012.
- [17] James B. Hartle. *Gravity: an introduction to Einstein’s general relativity.* Addison Wesley, America, 2003.
- [18] Einstein Radius. http://en.wikipedia.org/wiki/Einstein_radius, 2012.
- [19] Bernard Burchell. Analysis of Gravitational Lensing in Abell 1689. <http://www.alternativephysics.org/book/Abell1689.htm>, 2010.
- [20] Emma Grocutt. What is Gravitational Lensing? <http://www.cfhtlens.org/public/what-gravitational-lensing>, 2013.
- [21] Brice Ménard. Detecting and interpreting statistical lensing by absorbers. *The Astrophysical Journal*, pages 28–37, Sep 2005.
- [22] E. Mortsell and J. Jonsson. A model independent measure of the large scale curvature of the universe, 2011.
- [23] Dr. Edward J. Wollack. Measurements From WMAP. http://map.gsfc.nasa.gov/universe/uni_shape.html, 2012.
- [24] Cong Ma and Tong-Jie Zhang. Power of observational hubble parameter data: A figure of merit exploration. *The Astrophysical Journal*, 730(2):74, 2011.
- [25] E. Komatsu, K. M. Smith, J. Dunkley, C. L. Bennett, B. Gold, G. Hinshaw, N. Jarosik, D. Larson, M. R. Nolta, L. Page, D. N. Spergel, M. Halpern, R. S. Hill, A. Kogut, M. Limon,

- S. S. Meyer, N. Odegard, G. S. Tucker, J. L. Weiland, E. Wollack, and E. L. Wright. Seven-year wilkinson microwave anisotropy probe (wmap) observations: Cosmological interpretation. *The Astrophysical Journal Supplement Series*, 192(2):18, 2011.
- [26] David W. Hogg. Distance measures in cosmology, 1999.
- [27] Iribarrem, A. S., Lopes, A. R., Ribeiro, M. B., and Stoeger, W. R. Relativistic cosmology number densities and the luminosity function. *A&A*, 539:A112, 2012.
- [28] University of Virginia Department of Astronomy. Luminosity functions [online]. http://www.astro.virginia.edu/class/whittle/astr553/Topic04/Lecture_4.html, 2005.
- [29] Robert C., Kennicutt, F., and Schweizer, J.E. *Galaxies: Interactions and Induced Star Formation*. Springer, 1998.
- [30] D. Barry. Basic observational knowledge. <http://coursewiki.astro.cornell.edu/Astro4410/BasicObservationalKnowledge>, 2009.
- [31] Space Telescope Science Institute. http://hubblesite.org/the_telescope/hubble_essentials/quick_facts.php.
- [32] NASA. <http://solarsystem.nasa.gov/missions/profile.cfm?MCode=HST>, 2011.
- [33] Space Telescope Science Institute. http://hubblesite.org/hubble_discoveries/breakthroughs/planetary.
- [34] ESA. http://www.spacetelescope.org/science/deep_fields/.
- [35] Space Telescope Science Institute. http://hubblesite.org/hubble_discoveries/breakthroughs/cosmology.
- [36] R. J. Bouwens, P. A. Oesch, G. D. Illingworth, I. Labbé, P. G. van Dokkum, G. Brammer, D. Magee, L. R. Spitler, M. Franx, R. Smit, M. Trenti, V. Gonzalez, and C. M. Carollo. Photometric Constraints on the Redshift of $z \sim 10$ Candidate UDFj-39546284 from Deeper WFC3/IR+ACS+IRAC Observations over the HUDF. , 765:L16, March 2013.
- [37] Space Telescope Science Institute. http://hubblesite.org/the_telescope/nuts_.and_.bolts/spacecraft_systems/.
- [38] Space Telescope Science Institute. http://hubblesite.org/the_telescope/nuts_.and_.bolts/optics/.
- [39] ESA. http://www.spacetelescope.org/about/history/servicing_mission_1/.
- [40] Susan Watanabe. Fast facts. <http://www.spitzer.caltech.edu/info/277-Fast-Facts>, 2012.
- [41] Dan Coe, Adi Zitrin, Mauricio Carrasco, Xinwen Shu, Wei Zheng, Marc Postman, Larry Bradley, Anton Koekemoer, Rychard Bouwens, Tom Broadhurst, Anna Monna, Ole Host, Leonidas A. Moustakas, Holland Ford, John Moustakas, Arjen van der Wel, Megan Donahue, Steven A. Rodney, Narciso Benítez, Stephanie Jovel, Stella Seitz, Daniel D. Kelson, and Piero Rosati. Clash: Three strongly lensed images of a candidate $z \sim 11$ galaxy. *The Astrophysical Journal*, 762(1):32, 2013.
- [42] Johan Richard, Daniel P. Stark, Richard S. Ellis, Matthew R. George, Eiichi Egami, Jean-Paul Kneib, and Graham P. Smith. A hubble and spitzer space telescope survey for grav-

- itationally lensed galaxies: Further evidence for a significant population of low-luminosity galaxies beyond $z = 7$. *The Astrophysical Journal*, 685(2):705, 2008.
- [43] Ranga-Ram Chary, Daniel Stern, and Peter Eisenhardt. Spitzer constraints on the $z = 6.56$ galaxy lensed by abell 370. *The Astrophysical Journal Letters*, 635(1):L5, 2005.
- [44] J. Amos. Euclid telescope to probe dark universe. <http://www.bbc.co.uk/news/science-environment-18503703>, 2012.
- [45] Ref: EUCL-MPI-NPS-RP-00079. *NISP Performance Analysis Report*. 2012.
- [46] R. J. Bouwens, G. D. Illingworth, P. A. Oesch, I. Labbé, M. Trenti, P. van Dokkum, M. Franx, M. Stiavelli, C. M. Carollo, D. Magee, and V. Gonzalez. Ultraviolet Luminosity Functions from 132 $z \sim 7$ and $z \sim 8$ Lyman-break Galaxies in the Ultra-deep HUDF09 and Wide-area Early Release Science WFC3/IR Observations. , 737:90, August 2011.